buildings

MDPI

Article

Bond Performance between Fiber-Wrapped Ribbed Basalt Fiber-Reinforced Polymer Bars and Seawater Sea-Sand Concrete

Min Lin [1], Chenyue Weng [2], Hesheng Xiao [2], Dong Zeng [2], Baifa Zhang [3,*], Xiaopan Chen [3], Shaohua He [3] and Lijuan Li [3,*]

[1] School of Surveying, Mapping and Remote Sensing Information, Guangdong Polytechnic of Industry and Commerce, Guangzhou 510550, China; 0001200037@gdgm.edu.cn

[2] Guangdong Bocheng Construction Co., Ltd., Guangzhou 510660, China; 17818588537@163.com (C.W.); hill_2023@163.com (H.X.); baishikefa@163.com (D.Z.)

[3] School of Civil and Transportation Engineering, Guangdong University of Technology, Guangzhou 510006, China; 2112009109@mail2.gdut.edu.cn (X.C.); 1112209006@mail2.gdut.edu.cn (S.H.)

* Correspondence: zhangbaifa@gdut.edu.cn (B.Z.); lilj@gdut.edu.cn (L.L.)

Abstract: The high corrosion resistance of fiber-reinforced polymers (FRPs) and related concrete structures means that they are suitable for application in the marine environment. Therefore, the replacement of steel bars with fiber-reinforced polymer (FRP) bars enhances corrosion resistance in seawater sea-sand concrete (SSC) structures. Geometric parameters significantly influence the performance of the bond between ribbed FRP bars and SSC, thereby affecting the mechanical properties of the concrete structures. In this study, the performance of the bond between ribbed (i.e., with fiber wrapping) basalt-fiber-reinforced polymer (BFRP) bars and SSC was investigated through pull-out tests that considered rib geometry and SSC strength. The results demonstrated that an increase in rib and dent widths reduced the bond stiffness, while an increase in rib height and SSC strength gradually increased the bond stiffness and strength. Additionally, the bond stiffness and bond strength were relatively low because the surface fiber bundles buffered the mechanical interlocking force between the BFRP ribs and the concrete, resulting in plastic bond failure during the loading process. Furthermore, the adhesion of the fiber bundles to the surface of the BFRP bars also influenced bond performance, with higher adhesion leading to greater bond stiffness and strength.

Keywords: fiber wrapping; ribbed BFRP bar; rib geometry; seawater sea-sand concrete; bond stress–slip curve

Citation: Lin, M.; Weng, C.; Xiao, H.; Zeng, D.; Zhang, B.; Chen, X.; He, S.; Li, L. Bond Performance between Fiber-Wrapped Ribbed Basalt Fiber-Reinforced Polymer Bars and Seawater Sea-Sand Concrete. *Buildings* **2024**, *14*, 38. https://doi.org/10.3390/buildings14010038

Academic Editor: Flavio Stochino

Received: 18 November 2023
Revised: 8 December 2023
Accepted: 10 December 2023
Published: 22 December 2023

1. Introduction

The construction material industry consumes large amounts of freshwater, river sand, and other natural resources [1,2]. Approximately 20 billion tonnes of concrete is produced annually, and the production process requires the use of approximately 15 billion tonnes of aggregates and 1.8 billion tonnes of water [3,4]. The extensive consumption of freshwater has exacerbated its scarcity, and the extensive exploitation of river sand has caused damage to riverbeds [5,6]. To alleviate the environmental damage caused by concrete preparation, seawater and sea sand have been used to replace freshwater and river sand [7,8]. Several studies have reported the feasibility of using seawater and sea sand to prepare concrete with workability and mechanical properties similar to those of traditional concrete (TC). Wang et al. [9] found that seawater could enhance the hydration of ordinary Portland cement (OPC), resulting in a denser microstructure, higher crystal content, and reduced autogenous shrinkage. Pan et al. [10] compared the compressive behavior and microstructures of seawater sea-sand concrete (SSC), sea-sand concrete (SC), and TC. They found that the utilization of seawater and sea sand increased the early strength but reduced the late compressive strength of concrete, with seawater and sea sand inducing the formation of the ettringite phase. Fang et al. [11] investigated the axial compressive performance of square SSC columns reinforced with glass-fiber-reinforced polymer (FRP) interlocking multi-spirals and proposed a design-oriented load–strain model for predicting monotonic and cyclic axial responses of this structure. Other studies have found that the chloride and sulfate content in seawater and sea sand can accelerate the corrosion of steel bars in reinforced concrete structures, significantly reducing the bearing capacity and durability of concrete structures [12–14]. To address this issue, FRP bars are used to replace steel bars in SSC-based structures owing to their light weight, low thermal conductivity, and strong corrosion resistance [15].

FRP bars are produced by mixing fibers and polymeric materials through the pultrusion process, and have been extensively studied as a promising alternative for the construction of marine structures [7,16,17]. The strength of the bond between the bars and the concrete plays a significant role in the ultimate and serviceability limit states (e.g., anchorage length and crack width) of concrete structures [18]. The differing composition and physical properties of FRP and steel are reflected in their distinct bond behavior with concrete. Typically, bond strength is influenced by factors such as bond length, cover thickness, concrete strength, transverse compression, bar diameter, and surface-treatment methods [19–21]. Among these factors, the surface treatments (involving deformation, sand-coating, or combinations of both) of FRP bars are some of the most critical [22].

Deformed FRP bars exhibit better adhesion to concrete than sand-coated FRP bars owing to the excellent mechanical interlocking force of the former [23,24]. Furthermore, as depicted in Figure 1, deformed FRP bars can be further categorized into three types according to their production processes: (1) fiber-wrapped bars, in which ribs are formed by helically wrapped fibers (remaining in the bar) on the smooth bar [25]; (2) indented bars, in which ribs are formed via a helix cutting method on the smooth bar [26]; and (3) ribbed bars, which are formed by squeezing strands onto the smooth bar [27]. Ribbed bars can be divided into two types depending on the presence or absence of fiber. The behavior of bar–concrete bonding varies for these two types of ribbed bars. Hao et al. [28] found that the bonding behavior of ribbed (without fiber) glass FRP-bar-reinforced concrete was affected by rib parameters. Wei et al. [29] compared the bond performances of concretes reinforced with different fiber-wrapped ribbed FRP bars and concluded that carbon FRP bars showed the greatest bond strength and durability, while glass FRP bars exhibited the smallest bond strength, as the fibers were easily cut off and attached to the concrete interface.

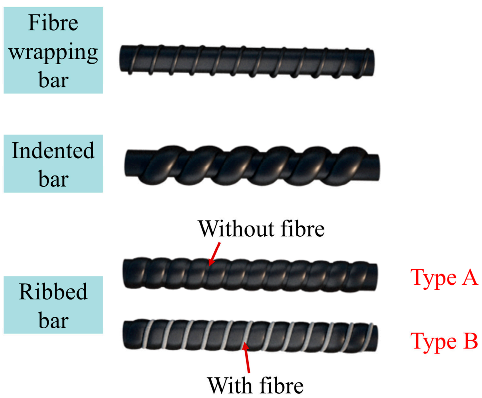

Figure 1. Three types of deformed FRP bar.

In addition to the treatment types, rib geometry, including dent width (DW), rib width (RW), rib height (RH), and rib spacing (RS), also has a significant effect on the behavior of the bond between FRP bars and concrete. Solyom and Balazs [26] reported that the bond strength of concrete reinforced with Type A ribbed glass FRP bars increased by 100% as the ratio of DW/RS increased from 0.17 to 0.30. Through finite element analysis, Sasmal et al. [30] found that a decrease in RS was beneficial in improving bond strength when RS was greater than 80% of the bar diameter. Shan et al. [31] reported that the bond strength of

Type A ribbed basalt FRP (BFRP) bars with concrete was significantly enhanced by a factor of 11 as the RH increased from 0 to 0.76 mm, and they proposed a novel bar-geometry-based model. Furthermore, bond failure between deformed FRP bars and concrete is also affected by the properties of the concrete and the geometry of the ribs on the FRP bars [32]. However, although existing research has confirmed that rib geometry has a significant effect on the bond performance between FRP bars and concrete, its influencing mechanism is still unclear, and the relevant theoretical models are not yet perfect [20,31,33]. For these reasons, in existing standards, the effects of rib geometry are not considered in calculating the development length. For example, Japan standard JSCE [34] and Canadian standard CSA S806 [35] only generally consider the effects of bar surface treatments in calculating the development length, without specific provisions for rib geometry. In the American standard [36], even the effects of bar surface treatment are not taken into account when calculating the development length. To determine the development, for FRP-bar-reinforced concrete structures, it is necessary to clarify the effects of rib geometry on the bond between the FRP bars and the concrete.

Fiber-wrapped ribbed bars have received less attention than ribbed bars without fiber. In our previous studies [37], we found that the damage to the bar ribs could be reduced by fiber floccules formed by strands damaged under friction. We have also observed that fiber-wrapped ribbed BFRP bars can undergo full deformation, unlike ribbed bars that do not have fiber wrapping, with the former showing higher bond strength than the latter. These results indicate that the presence of fiber in the rib favors the improvement of bond strength between the bars and the concrete. Therefore, clarifying the effects of rib geometry on the bond performance between the FRP bars and the concrete is necessary, especially for fiber-wrapped ribbed bars.

Among all the FRP bars, BFRP bars were used in this study because they are cost-effective and result in low pollution during manufacture [38,39]. In this study, we focused on the combination of FRP bars and concrete prepared with seawater sea sand, and especially on the effect of rib geometry (RW, DW, and RH of the ribbed bars) and concrete strength on the bond behavior (failure modes of the bond interface, bond stress–slip curves, and bond indexes) of the bonds between fiber-wrapped ribbed BFRP bars and SSC. These parameters are of great importance in promoting the application of SSC structures in the marine environment, and were studied in detail.

2. Experimental Programme

2.1. Seawater Sea-Sand Concrete (SSC)

OPC (P.O. 42.5R) was used as the binder. Its chemical composition, determined by X-ray fluorescence spectrometer, was as follows: SiO_2 (11.5 wt%), Al_2O_3 (2.5 wt%), CaO (76.2 wt%), Fe_2O_3 (3.9 wt%), K_2O (1.2 wt%), TiO_2 (0.6 wt%), SO_3 (3.7 wt%), and others (0.4 wt%). Both seawater and sea sand were collected at a shore in Zhuhai city, Guangdong (N22°13′; E113°33′) for use as mixed water and fine aggregates. The seawater mainly contained ions such as Na^+ (2500 mg/L), Cl^- (4126 mg/L), Mg^{2+} (981 mg/L), and $SO4^{2-}$ (379 mg/L). Crushed stones were used as coarse aggregates. The particle size distributions of fine and coarse aggregates are presented in Figure 2.

Following specification JGJ 55-2011 [40], we prepared SSC with three strength grades by adjusting the mix proportion of the concrete, as shown in Table 1. According to American standards ASTM C39/C39M [41] and ASTM C469/C469M [42], the compressive tests were carried out at the concrete age of 28 d. The compressive strengths were approximately 43, 58, and 68 MPa, and the elastic moduli were 26, 29, and 31 GPa, respectively.

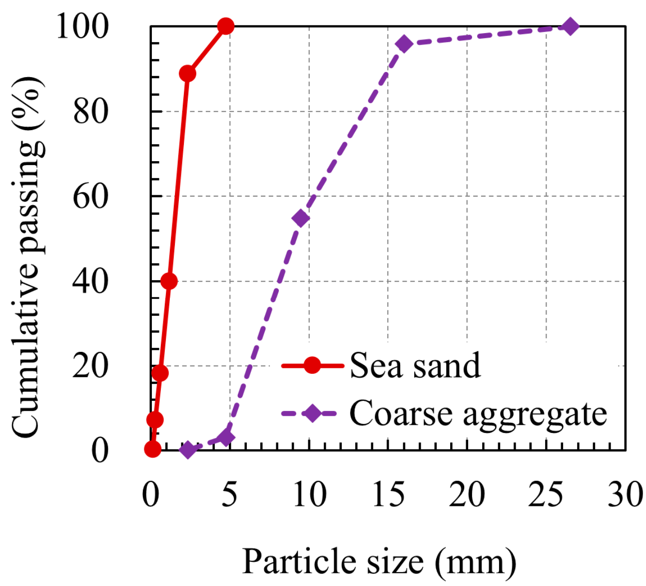

Figure 2. Particle size distributions of aggregates.

Table 1. Mix proportions of SSC.

Strength Grade	Cement (kg/m^3)	Seawater (kg/m^3)	Sea Sand (kg/m^3)	Coarse Aggregates (kg/m^3)
C30	400.83	230.00	721.82	1047.35
C45	540.07	230.00	573.57	1056.36
C60	686.50	230.00	438.82	1044.68

2.2. Ribbed BFRP Bars

Bar diameter, RW, DW, and RH are typically used to characterize rib geometry (Figure 3). In this study, fiber-wrapped ribbed BFRP bars with a nominal diameter of 10 mm were selected, and the effects of rib geometry on the mechanical properties of BFRP-reinforced SSC were investigated. The detailed rib geometry (with an error of <5%) and mechanical properties (tensile strength and elastic modulus) of the ribbed BFRP bars are listed in Table 2. The samples are denoted as $W_XD_YH_Z$ or $W_XD_YH_Z$-C_G, where X, Y, and Z represent the values of RW, DW, and RH, respectively. -C_G indicates different SSC strengths, and G represents the concrete grade. Notably, those sample IDs without -C_G indicate that the concrete strength was 45 MPa.

Table 2. Detailed rib geometry and mechanical properties of ribbed BFRP bars.

No.	Sample ID	Diameter (mm)	Rib Width (mm)	Dent Width (mm)	Rib Height (mm)	Equivalent Diameter (mm)	Tensile Strength (Mpa)	Elastic Modulus (Gpa)
1	$W_{1.5}D_{2.5}H_{0.6}$	10.67	1.60	2.68	0.61	10.98	1069.52	43.29
2	$W_{3.5}D_{2.5}H_{0.6}$	10.70	3.63	2.52	0.61	11.18	1089.95	47.20
3	$W_{5.5}D_{2.5}H_{0.6}$	10.61	5.69	2.67	0.63	11.18	1218.84	44.40
4	$W_{7.0}D_{2.5}H_{0.6}$	10.15	7.14	2.78	0.68	11.06	1158.43	44.08
5	$W_{7.5}D_{2.0}H_{0.7}$	10.75	7.65	2.06	0.67	11.45	975.86	43.34
6	$W_{7.5}D_{3.0}H_{0.7}$	10.35	7.90	2.97	0.73	10.80	1305.98	41.59
7	$W_{7.5}D_{3.3}H_{0.7}$	10.55	8.05	3.31	0.71	11.22	1012.06	44.78
8	$W_{7.5}D_{3.0}H_{0.4}$	10.18	7.52	2.83	0.45	10.62	1006.58	42.76
9	$W_{7.5}D_{3.0}H_{1.0}$	10.45	8.09	2.75	1.01	11.46	997.86	46.08
10	$W_{7.5}D_{3.0}H_{1.7}$	10.66	7.51	3.39	1.70	12.22	967.64	35.14
11	$W_{7.5}D_{3.0}H_{0.7}$-C_{30}	10.35	7.90	2.97	0.73	10.80	1305.98	41.59
12	$W_{7.5}D_{3.0}H_{0.7}$-C_{60}	10.35	7.90	2.97	0.73	10.80	1305.98	41.59

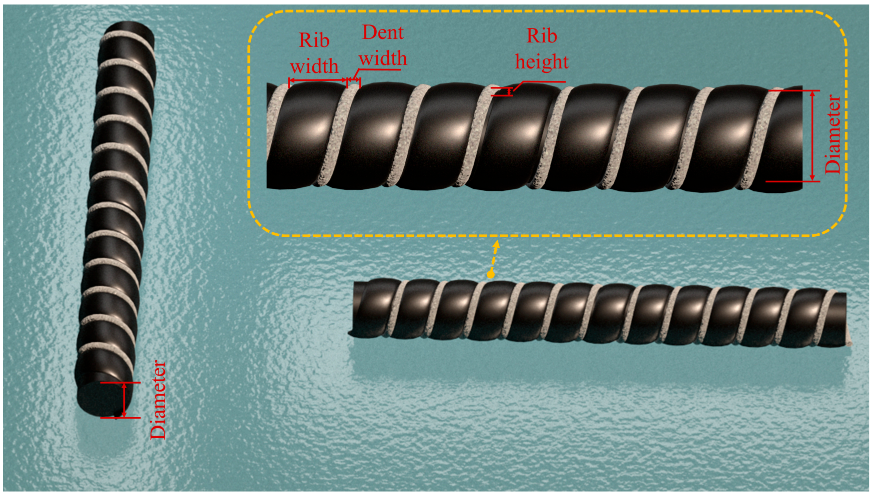

Figure 3. Geometric details of fiber-wrapped ribbed BFRP bars.

2.3. Specimen Preparation

The process used to prepare specimens is shown in Figure 4, and the detailed preparation process can be found in our previous study [7]. The preparation of SSC was divided into two steps: (I) the sea sand, coarse aggregates, and 70% of seawater were poured into the mixer and mixed for 30 s, and (II) the cement and the remaining seawater were poured in the mixer and mixed for 60 s. The size of the SSC cube was 200 × 200 × 200 mm^3, and the BFRP bar was 550 mm in length. Three replicates were prepared and tested for each sample. These pull-out specimens were cured for 28 days in a room with a temperature of 20 ± 3 °C and a humidity of 95%.

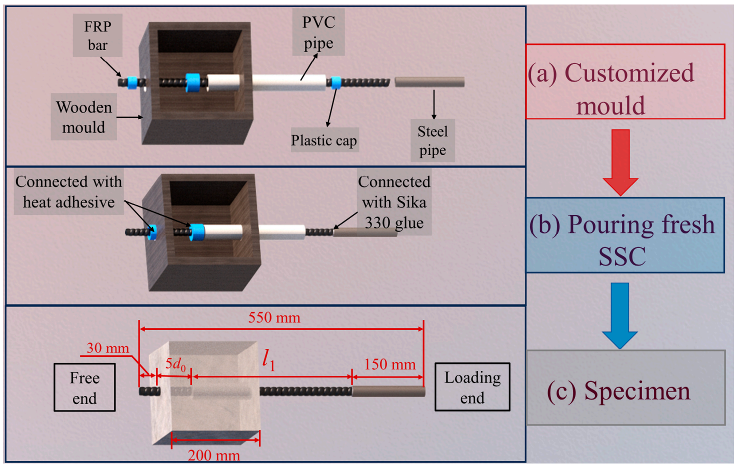

Figure 4. Specimen preparation process. (**a**) customized mould; (**b**) pouring fresh SSC; (**c**) Specimens.

2.4. Test Setup

A Matest 330 testing machine was used to test the pull-out behavior of SSC reinforced with fiber-wrapped ribbed BFRP. The specimens were covered with gypsum at the bottom to level the contact surface and reduce friction. According to American standard ACI 440.3R-12 [43], a displacement rate of 1.2 mm/min was applied during the loading, and the test was stopped when the displacement distance exceeded 20 mm. It is assumed that the bond stress is evenly distributed along the bonded length, so bond stress (τ) was calculated by Equation (1). The slip between the BFRP bar and SSC at the loading end (s) was calculated by Equation (2).

$$\tau = \frac{F}{\pi d_0 l_b} \quad (1)$$

$$s = \frac{s'EA - l_1F}{F + EA} \tag{2}$$

where A, E, and d_0 represents the cross-sectional area, elastic modulus, and equivalent diameter of the BFRP bar, respectively; F is the loading force; l_b is the bond length, which equals $5d_0$; s' is the displacement at the position of the steel pipe in Figure 4; and l_1 is the length in Figure 4.

3. Experimental Results and Discussions

3.1. Failure Modes of the Bond Interface between Bars and SSC

All specimens were split to observe the failure modes of the bond interface (Figure 5). All of these specimens experienced pull-out failure, and the rib geometry and SSC strength had little effect on the bond interface failure mode of the specimens. The appearances of different fiber-wrapped ribbed BFRP bars after the pull-out test were similar: crushed concrete was embedded on the surface of the fibers and ribs, the fibers were destroyed, and flocculent fibers were attached to the concrete surface.

As the RW and DW increased, the presence of damaged white fiber became more apparent, both on the bar's surface and in the concrete, because a wider rib or dent allowed more room for fiber slippage. Increasing the concrete strength also resulted in more noticeable peeled fiber, owing to the increased bonding strength between the concrete and bars [44]. With increasing RH, the amount of flocculent fiber in the concrete decreased, and the concrete was more severely damaged.

Despite these observations, the specimens could be categorized into two types according to the damage to the interface.

The first type exhibited brittle-fracture failure of the ribs, including the peeling of ribs from BFRP bars and the shearing of the concrete ribs. This was often accompanied by the breakage or severe wear of entangled fibers on the bar's surface (as in samples $W_{7.5}D_{3.3}H_{0.7}$, $W_{7.5}D_{3.0}H_{0.7}$, $W_{7.5}D_{3.0}H_{1.0}$, $W_{7.5}D_{3.0}H_{1.7}$, and $W_{7.5}D_{3.0}H_{1.7}$-C_{60}). The second type had ribs with a relatively intact shape (as seen in samples $W_{1.5}D_{2.5}H_{0.6}$, $W_{7.5}D_{3.0}H_{0.4}$, and $W_{7.5}D_{3.0}H_{1.7}$-C_{30}), in which only deformed and worn ribs occurred, owing to the compressive interaction between the BFRP bars, the wrapped fiber bundles, and the concrete.

The primary forces between fiber-wrapped BFRP bars and concrete are chemical adhesion, friction, and mechanical interlocking force [24]. During the initial loading stage, the bond stress was mainly provided by the chemical adhesion [33]. However, the chemical adhesive force disappeared once a slight slip occurred, owing to the separation of bars and concrete [45]. At this stage, relative slip between BFRP bars and concrete occurred on the inclined plane where their ribs came into contact (Figure 6). Simultaneously, the concrete was both sheared and compressed by the component forces along the pulling and vertical directions of the ribs [46]. Compared with the threaded surface of BFRP bars under similar conditions, the fiber wrapping around the dents reduced the gap between the BFRP bars and the concrete, significantly cushioning the strong mechanical interlocking effect in the bonding section, thus favoring the integrity of both the BFRP and the concrete ribs [33].

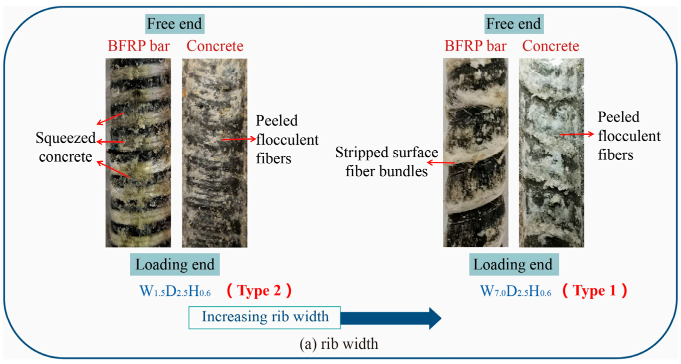

Figure 5. *Cont.*

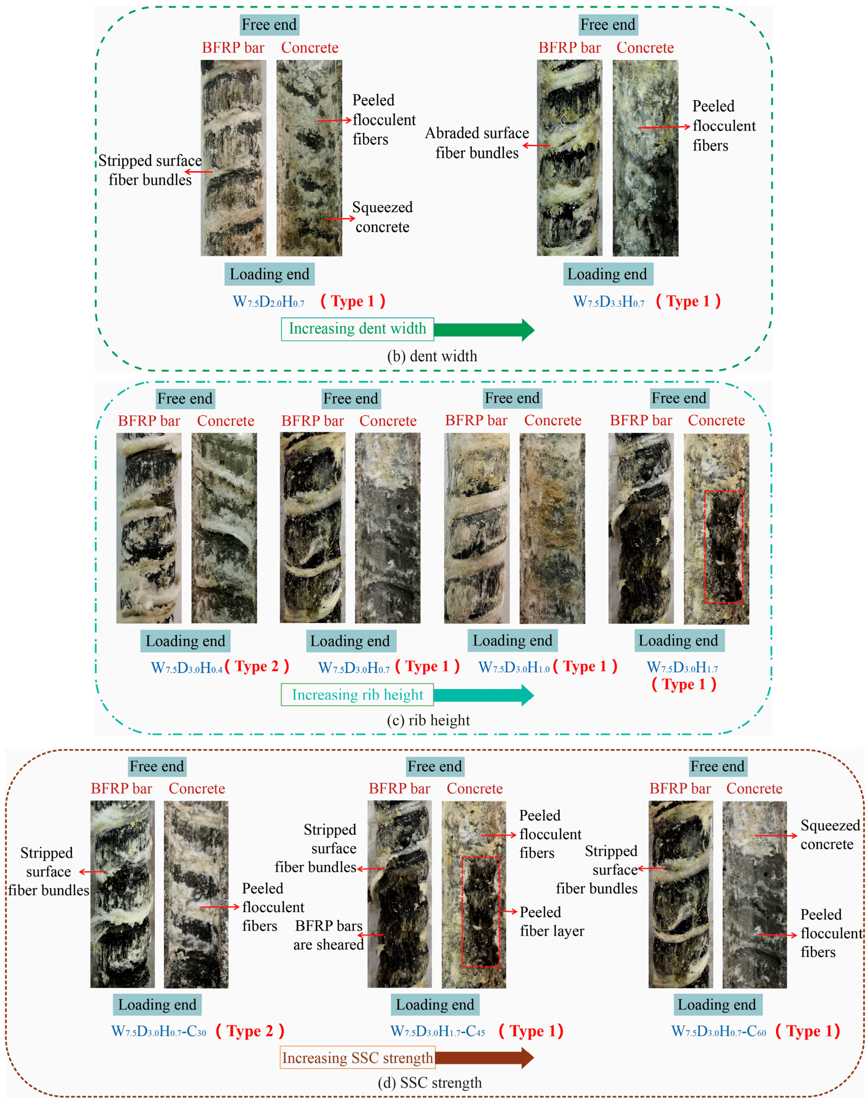

Figure 5. Failure modes of the bond interface between fiber-wrapped BFRP bars and SSC: (**a**) RW, (**b**) DW, (**c**) RH, and (**d**) SSC strength.

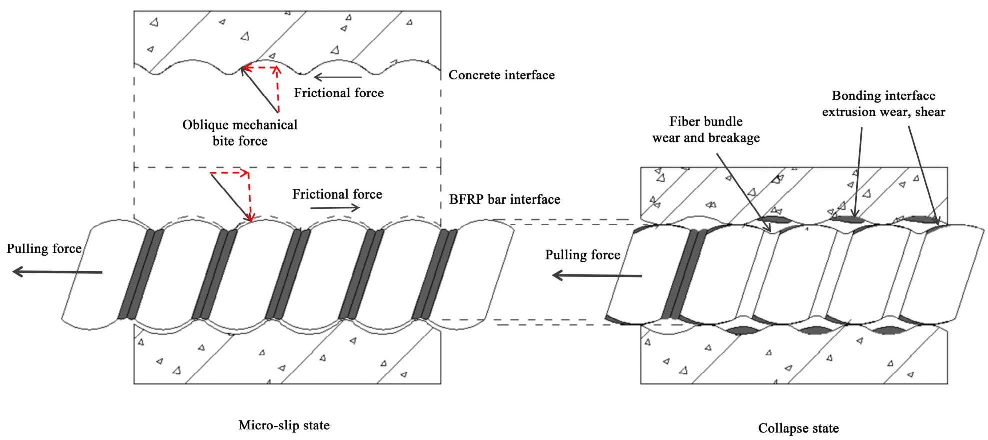

Figure 6. Bond mechanism between a fiber-wrapped BFRP bar and SSC.

As the pulling force increased further, the fibers and ribs of the BFRP and the concrete began to suffer damage owing to their relative slip. The deformed ribs of the BFRP bars and concrete interlocked, increasing the bond stress. However, with the accumulation of stress between the BFRP bar and the concrete, brittle-fracture failure of the ribs might occur when this stress surpasses the shear strength of either the BFRP bar's or the concrete's ribs. Moreover, the surface fibers were severely worn and broken, accompanied by a rapid degradation of the mechanical interlocking force until the bond ultimately failed. In cases in which the stress between the BFRP bar and the concrete did not exceed the shear strength of the ribs, the bar and concrete showed deformation and wear owing to mutual extrusion [8].

3.2. Bond Stress–Slip Curves

Figure 7 displays the bond stress–slip curve of BFRP-bar-reinforced SSC at varying rib geometries and concrete strengths. The curve can be categorized into three types:

Case 1, the bond stress–slip curve of $W_{7.5}D_{3.0}H_{0.5}$ can be divided into two parts—the ascending and descending parts (Figure 7a,m). The ascending part of the curve exhibited elastic characteristics, with slip increasing as stress increased. However, as slip continued to increase, bond damage occurred, and the curve entered a nonlinear upward phase. During this stage, the bonding stiffness of the BFRP-bar-reinforced concrete gradually decreased until it reached zero, while the bonding stress reached its maximum value. Afterward, the stress began to decline, and the slip continued to increase. In this phase, the bonding stress decreased rapidly until it reached zero.

Case 2, the bond stress–slip curve of $W_{7.0}D_{2.5}H_{0.6}$, $W_{7.5}D_{3.0}H_{0.7}$, $W_{7.5}D_{3.3}H_{0.7}$, $W_{7.5}D_{3.0}H_{0.4}$ $W_{7.5}D_{3.0}H_{1.7}$, $W_{7.5}D_{3.0}H_{0.7}$-C_{30}, and $W_{7.5}D_{3.0}H_{0.7}$-C_{60} can be divided into ascending, descending, and residual parts (Figure 7o). In the ascending part, the bonding stress increased rapidly owing to the high bond stiffness. After the bond stress reached its maximum value, it decreased significantly but did not reach zero, because the rib of the free end of the BFRP bar entered the bonding section, providing a new mechanical interlocking force before the bond stress dropped to zero. Subsequently, the bond stress–slip curve entered the residual part. Owing to the protection from the surface fiber bundles, mechanical occlusion between the bars and concrete remained the main effect in the residual stage. However, the bond stiffness and bond stress in the residual part were smaller than those in the ascending part owing to the accumulation of bond damage, resulting in a reduction in mechanical interlocking force [29].

Case 3, the bond stress–slip curve of $W_{1.5}D_{2.5}H_{0.6}$, $W_{3.5}D_{2.5}H_{0.6}$, $W_{5.5}D_{2.5}H_{0.6}$, and $W_{7.5}D_{2.0}H_{0.7}$ was also divided into three parts—ascending, descending, and residual parts (Figure 7n). In the ascending stage, the bond stress–slip curve rose linearly. As slip increased, bond damage occurred, and the curve entered a nonlinear rising stage. The bonding stiffness gradually decreased until it reached zero, and the bonding stress reached its peak. Subsequently, the curve entered the second stage (descending stage). In this stage, the bond stress decreased with increasing slip owing to the compression deformation and wear between BFRP ribs, surface fiber bundles, and concrete ribs, corresponding to plastic characteristics. Similar to Case 2, the stress–slip curve entered a residual stage after a rib of the BFRP bar at the free end entered the bonding part.

Changes in the rib geometry altered the shape of the bond stress–slip curve for these samples. For example, when the RW increased from 5.5 to 7.0 mm, the type of bond stress–slip curve transformed from Case 3 to Case 2. The effects of rib geometry and SSC strength on bond stiffness, bond strength, slip, and residual strength and slip were further investigated.

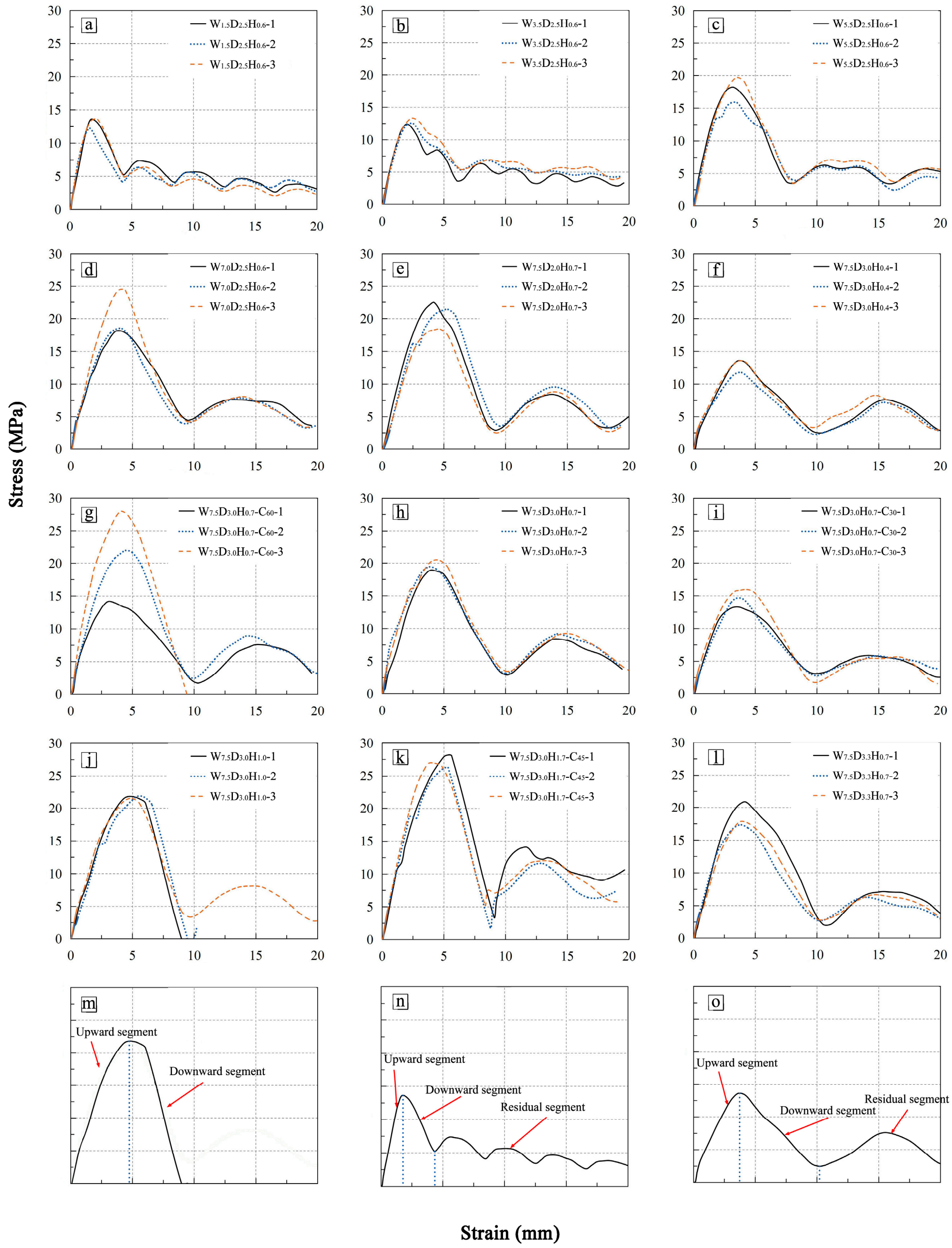

Figure 7. Bond stress–slip curves of all samples. (**a**) $W_{1.5}D_{2.5}H_{0.6}$; (**b**) $W_{3.5}D_{2.5}H_{0.6}$; (**c**) $W_{5.5}D_{2.5}H_{0.6}$; (**d**) $W_{7.0}D_{2.5}H_{0.6}$; (**e**) $W_{7.5}D_{2.0}H_{0.7}$; (**f**) $W_{7.5}D_{3.0}H_{0.4}$; (**g**) $W_{7.5}D_{3.0}H_{0.7}$-C_{60}; (**h**) $W_{7.5}D_{3.0}H_{0.7}$; (**i**) $W_{7.5}D_{3.0}H_{0.7}$-C_{30}; (**j**) $W_{7.5}D_{3.0}H_{1.0}$; (**k**) $W_{7.5}D_{3.0}H_{1.7}$-C_{45}; (**l**) $W_{7.5}D_{3.3}H_{0.7}$; and typical model: (**m**) Case 1; (**n**) Case 2; (**o**) Case 3.

3.3. Bond-Index Analysis

3.3.1. Bond Stiffness

In the bond stress–slip curve, the secant value at a slip of 0.5 mm was defined as the bond stiffness. Figure 8 illustrates the influence of rib geometry and SSC strength on bond stiffness.

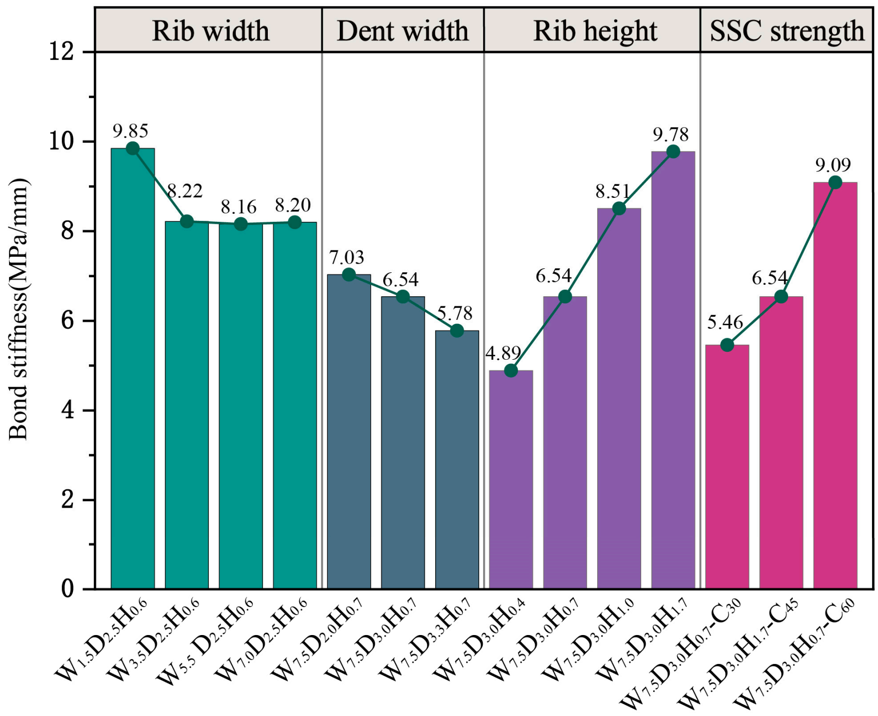

Figure 8. Bond stiffness of all samples.

Bond stiffness was highest (9.84 MPa/mm) when the RW was 1.5 mm. However, increasing the RW reduced the bond stiffness, and the bond stiffness values (approximately 8.20 MPa/mm) under RW values of 3.5, 5.5, and 7.0 mm were similar. This was attributable to the following: (1) Bond stiffness was affected by the contact angle of the inclined plane between the BFRP rib and the concrete, which is inversely proportional to the RW. When the RW was 1.5 mm, the inclination angle was at its maximum. (2) The smaller width of the BFRP ribs resulted in more concrete ribs within a certain bonding length. Consequently, the number of biting surfaces between the BFRP ribs and the concrete also increased. Therefore, 1.5 mm-width ribs exhibited greater mechanical interlocking force and bonding stiffness than other ribs owing to the combined effect of the above factors.

In addition, the increase in the DW also reduced the bond stiffness. However, the changes in DWs were caused by different processing technologies for fiber-wrapped BFRP bars. For example, only a thick fiber bundle was wrapped around the surface of the BFRP bar with a DW of 2.0 mm, whereas two thin fiber bundles of 3.0 and 3.3 mm were used in other cases. Therefore, in addition to the DW, the occurrence of different fiber thicknesses also influenced the bond stiffness. According to the bond interface damage (Figure 5b), the decrease in bond stiffness was likely due to the presence of gaps between the fiber and dent when the DW increased; the presence of gaps reduced the frictional force. Therefore, the higher the adhesion of the fiber bundles on the surface of BFRP bars in the dents, the greater the bonding stiffness and the better the bonding performance.

As shown in Figure 8, the bond stiffness increased from 4.89 to 9.78 MPa/mm as the RH increased from 0.61 to 1.7 mm. This was also attributable to the angle (which is proportionate to the RH) of the inclined plane between the BFRP rib and the concrete. A larger angle leads to a greater mechanical interlocking force and, consequently, greater bond stiffness. As the RH increased from 0.7 to 1.0 mm, the failure mode transformed into brittle-fracture failure owing to the shearing of the BFRP bars.

Figure 8 also shows that the bond stiffness increased with the increase in concrete strength. Higher concrete strength reduced the deformation capacity and thus increased the mechanical interlocking force [47]. When the concrete strength reached C60, the failure mode of the sample transformed into brittle-fracture failure.

3.3.2. Bond Strength and Bond Slip

The peak bond stress on the bond stress–slip curve was defined as the bond strength ($\tau_{b,x}$), and the slip corresponding to this bond strength was the bond slip ($s_{b,x}$).

Figure 9 illustrates the influence of rib geometry and SSC strength on the bond strength. The increased RW favored the bond strength, which increased to 20.34 MPa as the RW increased to 7.0 mm. Although the number of ribs and the slope decreased as the RW increased, the presence of fiber enhanced the bond strength. This was also supported by the similar bond stiffness but increased bond slip.

Figure 9 also shows that the bond strength decreased with the increase in DW. As the DW increased from 2.0 to 3.3 mm, the bond strength decreased by 13.89% because the number of bar ribs per unit bond length reduced with the increase in DW.

The increase in RH and SSC strength increased the bond strength, which was attributable to the increase in mechanical interlocking force between the BFRP bar and the SSC. Regarding the RH, the increased slope caused by the increasing RH resulted in greater bond strength [48]. For the SSC, where bond failure mainly occurred, increasing SCC strength enhanced the bond strength.

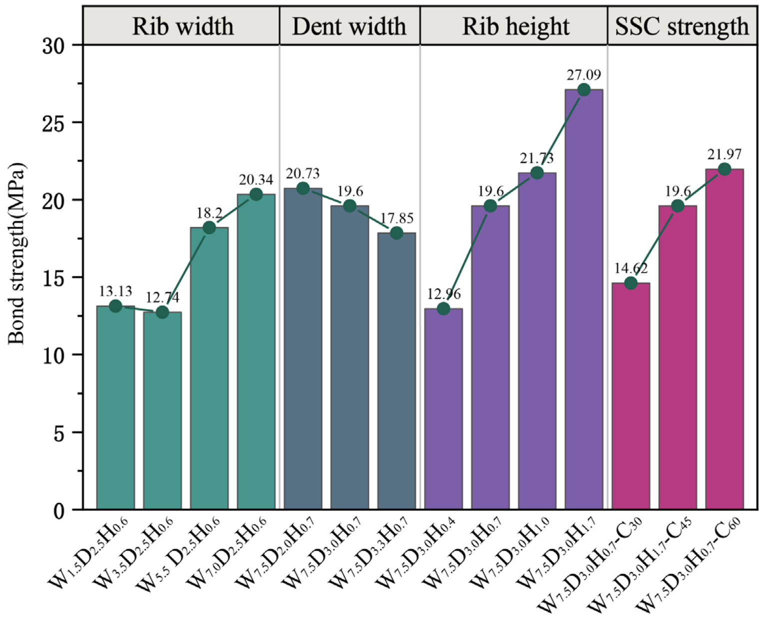

Figure 9. Bond strength of all samples.

Figure 10 illustrates the influence of rib geometry and SSC strength on the bond slip. The bond slip increased with increases in the RW and the RH. For example, as the RW increased from 1.5 to 7.0 mm, the bond slip increased from only 1.75 to 3.94 mm. As the RH increased from 0.4 to 1.7 mm, the bond slip increased by 37.1%. In addition, the increase in DW decreased the bond slip. However, the bond slip appeared to be not significantly affected by the changes in concrete strength. As the concrete strength increased from C30 to C60, the bond slip remained at ~3.90 mm.

Similar to the case of Type A BFRP-bar-reinforced SSC, bond strength reached its maximum value once the contact occurred at the highest point of the BFRP rib and the SSC, where the BFRP bar was pulled to approximately ½ of the actual RS (rib width (W) + dent width (D)). However, for a fiber-wrapped BFRP bar, the thickness of the fiber bundle and the snugness of the winding should be considered, not just the W and D values.

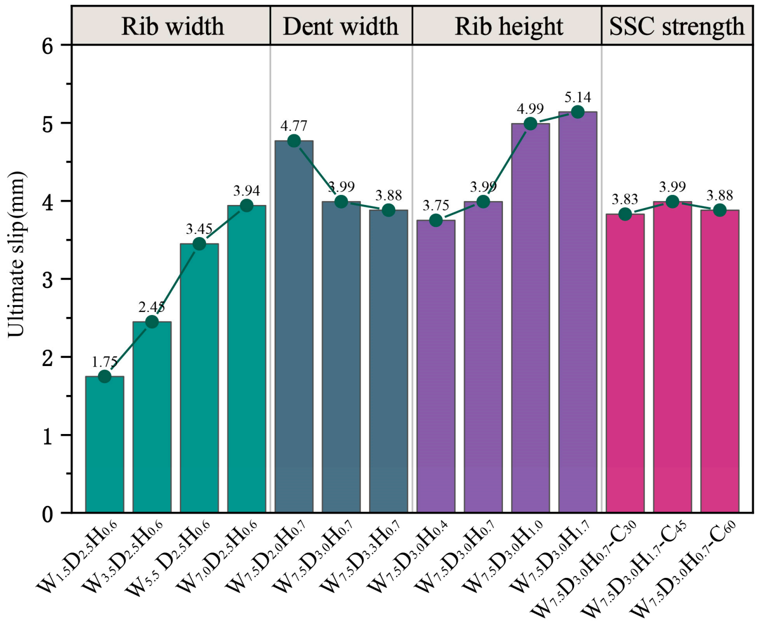

Figure 10. Bond slip of all samples.

3.3.3. Residual Bond Strength and Bond Slip

Figure 11 shows the influence of rib geometry and SSC strength on the residual bond strength. As the RW increased from 1.5 to 5.5 mm, the residual bond strength decreased. However, as the RW further increased to 7.0 mm, the residual bonding strength increased. Additionally, when the DW increased from 2.0 to 3.3 mm, the residual bond strength initially increased and then decreased, but to a small extent. In addition, the residual bond strength increased with the increase in RH. As for the increasing concrete strength, the residual bond strength first increased and then decreased. For the SSC reinforced with fiber-wrapped BFRP bars, the changes in bond strength in response to the changes in the rib geometry and SSC strength were complex because the factors influencing the reduction of the wedge cone were complex. These factors included the height of the remaining BFRP bar, the height of the SSC ribs, and the two slip interfaces.

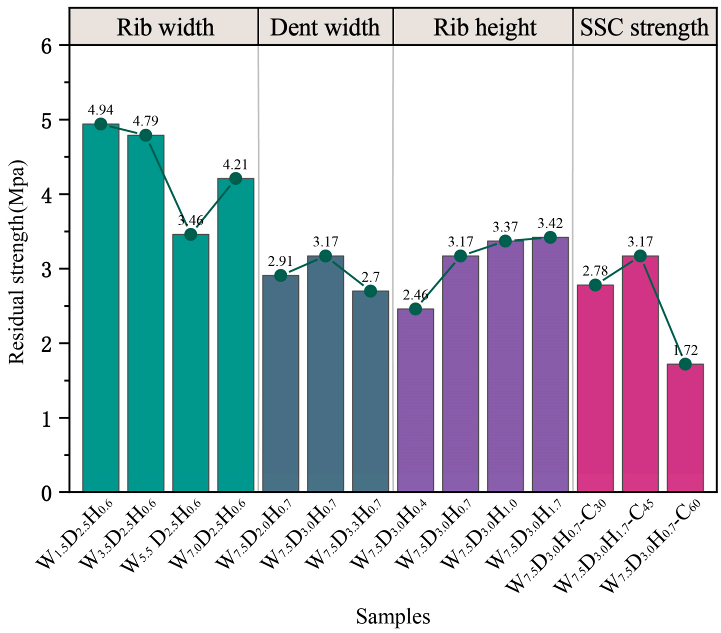

Figure 11. Residual bond strength of all samples.

Figure 12 shows that the residual bond slip increased with the increase in the RW and the DW but slightly decreased with the increase in RH. The concrete strength appeared to have little effect on the residual bond slip, with the residual bond slip being ~10.0 mm. For example, the residual bond slips increased by 119.77% and 12.39% as the RW increased from 1.5 to 7.0 mm and as the DW increased from 2.0 to 3.3 mm, respectively. According to the pull-out mechanism, the residual slip marked both the end of the former slip and the beginning of the next slip process, which was approximately one concrete rib distance, i.e., (W + D). Therefore, the changes in RW and DW had a more significant effect on the bond residual slip than the RH and SSC strength. For fiber-wrapped BFRP bars, the thickness of the fiber bundle and the snugness of the winding should be considered, not just the W and D values.

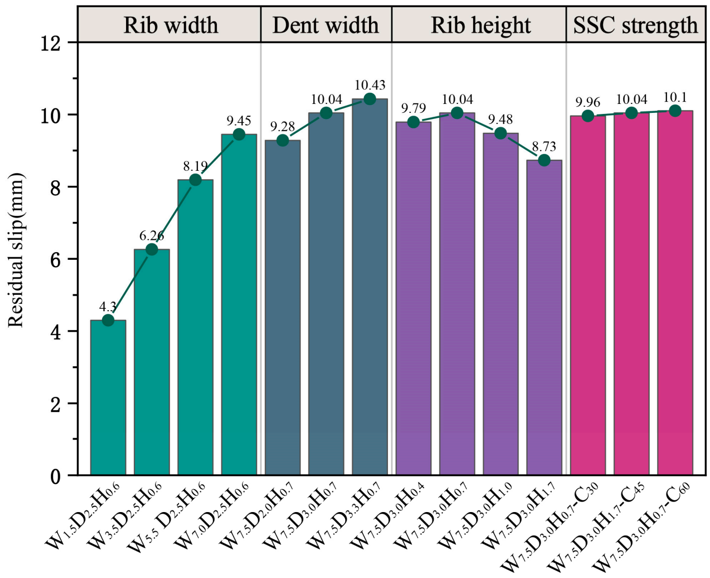

Figure 12. Residual bond slip of all samples.

Therefore, the increased dent width generally decreased the bond stiffness and residual strength but increased the bond strength and the ultimate and residual slips due to the greater width of the rib. The increased dent width also decreased bond stiffness, but increased the residual strength and slip. Meanwhile, the bond strength was also decreased. In fact, the dent width affected the technology process of the fiber-wrapped BFRP bar, causing the different fiber thicknesses and complicated interaction between the bars and the SSC. In contrast, the increase in rib height increased most of the bond indexes, including bond stiffness, bond strength, residual strength, and ultimate slip owing to the increasing interlocking strength. Consequently, the residual slip was also decreased. In addition, the increased concrete strength increased the bond stiffness and strength significantly, but had little effect on the bond and residual slip. This is because the interaction between bars and SSC was improved by increasing the strength of the SSC.

4. Conclusions

This study focused on the performance of the bond between fiber-wrapped BFRP bars and seawater sea-sand concrete (SSC) under different rib geometries and concrete strengths. Through the pull-out test, their bond behavior was investigated.

Geometric parameters had a significant effect on the bond index of BFRP bars and SSC. The increase in rib width decreased the bond stiffness from 9.85 to 8.20 MPa/mm but increased the bond strength from 13.13 to 20.34 MPa. The ultimate slip and residual slip were also increased owing to changes in the number of ribs. The increase in the dent width (DW) reduced the bond stiffness, bond strength, and bond slip. This change was related not only the DW but also to the adhesion of the fiber bundles on the surface of the BFRP bars, which was related to the processing technology. In fact, the fiber also significantly affected the bond performance of BFRP-bar-reinforced SSC. The fiber wrapped on the surface of rib could, to a certain extent, protect against the destruction of the bar. In particular, the processing technology and wrapping type resulting from different DWs significantly affected the failure mode of the SSC. The increase in both rib height (RH) and SSC strength contributed to the improvement of bond stiffness and bond strength owing to the enhancement of the mechanical interlocking force. The increase in RH also increased the bond slip and residual strength. However, the changes in bond slip, residual slip, and residual strength due to changes in SSC strength were complicated because of the low water content during hydration.

According to the bond interface damage, the specimens could be divided into two categories. One was characterized by the brittle-fracture failure of the ribs, which included the detachment of BFRP bar ribs and the shearing of the concrete ribs, accompanied by the collapse or severe wear of the surface-wrapped fiber bundles. The other category was categorized by deformation and wear caused by the compression between the ribs of BFRP bars, the surface-wrapped fiber bundles, and the concrete ribs. By altering the geometric parameters of the BFRP bars and the SSC strength, the bond performance, including bond interface damage, and the bond index could be controlled.

These findings show the relationship between the geometric parameters of fiber-wrapping rib and its bond strength in seawater sea-sand concrete, and provide an understanding of bond behavior of fiber-wrapped ribbed BFRP bars and seawater sea-sand concrete.

Author Contributions: Conceptualization, M.L., C.W. and L.L.; data curation, B.Z., D.Z. and L.L.; formal analysis, X.C.; funding acquisition, L.L. and M.L.; investigation, H.X.; methodology, S.H. and B.Z.; project administration, L.L. and M.L.; resources, L.L.; software, C.W.; supervision, S.H. and L.L.; writing—original draft, M.L. and X.C.; writing—review and editing, H.X., D.Z. and L.L. All authors have read and agreed to the published version of the manuscript.

Funding: This research was funded by the Guangzhou Science and Technology Plan Project (Grant No. 202201011636), the 2022 Higher Education Science Research Plan Project (Grant No. 22GDZY0105), the 2021 Academic Ideological and Political Education Project of Guangdong Provincial Department of Education (Grant No. 2021GXSZ143), and the National Natural Science Foundation of China (Grant No. 12032009).

Data Availability Statement: The original data are available upon request. The data are not publicly available due to the project privacy.

Acknowledgments: The authors gratefully thanks all technical personnel from the Structural Laboratory of Guangdong University of Technology for their assistance during the experiment.

Conflicts of Interest: Authors Chenyue Weng, Hesheng Xiao and Dong Zeng were employed by the company Guangdong Bocheng Construction Co., Ltd. The remaining authors declare that the research was conducted in the absence of any commercial or financial relationships that could be construed as a potential conflict of interest.

References

1. Gautam, L.; Bansal, S.; Sharma, K.V.; Kalla, P. Bone-china ceramic powder and granite industrial by-product waste in self-compacting concrete: A durability assessment with statistical validation. *Structures* **2023**, *54*, 837–856. [CrossRef]
2. Gautam, L.; Kalla, P.; Jain, J.K.; Choudhary, R.; Jain, A. Robustness of self-compacting concrete incorporating bone china ceramic waste powder along with granite cutting waste for sustainable development. *J. Clean. Prod.* **2022**, *367*, 132969. [CrossRef]
3. Shirani, S.; Cuesta, A.; Morales-Cantero, A.; Santacruz, I.; Diaz, A.; Trtik, P.; Holler, M.; Rack, A.; Lukic, B.; Brun, E.; et al. 4D nanoimaging of early age cement hydration. *Nat. Commun.* **2023**, *14*, 2652. [CrossRef]
4. Habert, G.; Miller, S.A.; John, V.M.; Provis, J.L.; Favier, A.; Horvath, A.; Scrivener, K.L. Environmental impacts and decarbonization strategies in the cement and concrete industries. *Nat. Rev. Earth Environ.* **2020**, *1*, 559–573. [CrossRef]
5. Salehi, M. Global water shortage and potable water safety; Today's concern and tomorrow's crisis. *Environ. Int.* **2022**, *158*, 106936. [CrossRef]
6. Rentier, E.; Cammeraat, L. The environmental impacts of river sand mining. *Sci. Total. Environ.* **2022**, *838*, 155877. [CrossRef]
7. Xiong, Z.; Mai, G.; Qiao, S.; He, S.; Zhang, B.; Wang, H.; Zhou, K.; Li, L. Fatigue bond behaviour between basalt fibre-reinforced polymer bars and seawater sea-sand concrete. *Ocean Coast. Manag.* **2022**, *218*, 106038. [CrossRef]

8. Zhang, B.; Zhu, H.; Cao, R.; Ding, J.; Chen, X. Feasibility of using geopolymers to investigate the bond behavior of FRP bars in seawater sea-sand concrete. *Constr. Build. Mater.* **2021**, *282*, 122636. [CrossRef]
9. Wang, J.; Liu, E.; Li, L. Multiscale investigations on hydration mechanisms in seawater OPC paste. *Constr. Build. Mater.* **2018**, *191*, 891–903. [CrossRef]
10. Pan, D.; Yaseen, S.A.; Chen, K.; Niu, D.; Leung, C.K.Y.; Li, Z. Study of the influence of seawater and sea sand on the mechanical and microstructural properties of concrete. *J. Build. Eng.* **2021**, *42*, 103006. [CrossRef]
11. Fang, S.; Li, L.; Lin, L.; Wang, H.; Fang, Z.; Li, Z.; Xiong, Z.; Liu, F. FRP interlocking multi-spiral reinforced square concrete columns: A promising compression application for marine engineering. *Eng. Struct.* **2021**, *244*, 112733. [CrossRef]
12. Pan, D.; Niu, D.; Li, Z. Corrosion products of low-alloy steel bars and their induction of cracking in seawater sea-sand concrete cover. *Constr. Build. Mater.* **2023**, *389*, 131800. [CrossRef]
13. Dong, Z.; Han, T.; Ji, J.; Zhu, H.; Wu, G. Durability of discrete BFRP needle-reinforced seawater sea-sand concrete-filled GFRP tubular columns in the ocean environment. *Constr. Build. Mater.* **2023**, *365*, 130017. [CrossRef]
14. Xu, J.; Wu, Z.; Cao, Q.; Yu, R.C. Eccentric compression behavior of seawater and sea sand concrete columns reinforced with GFRP and stainless steel bars. *Eng. Struct.* **2023**, *291*, 116486. [CrossRef]
15. Bakis, C.E.; Bank, L.C.; Brown, V.L.; Cosenza, E.; Davalos, J.F.; Lesko, J.J.; Machida, A.; Rizkalla, S.H.; Triantafillou, T.C. Fiber-Reinforced Polymer Composites for Construction—State-of-the-Art Review. *J. Compos. Constr.* **2002**, *6*, 73–87. [CrossRef]
16. Ahmed, A.; Guo, S.; Zhang, Z.; Shi, C.; Zhu, D. A review on durability of fiber reinforced polymer (FRP) bars reinforced seawater sea sand concrete. *Constr. Build. Mater.* **2020**, *256*, 119484. [CrossRef]
17. Bai, Y.-L.; Yan, Z.-W.; Ozbakkaloglu, T.; Gao, W.-Y.; Zeng, J.-J. Mechanical behavior of large-rupture-strain (LRS) polyethylene naphthalene fiber bundles at different strain rates and temperatures. *Constr. Build. Mater.* **2021**, *297*, 123786. [CrossRef]
18. Yan, Z.-W.; Bai, Y.-L.; Ozbakkaloglu, T.; Gao, W.-Y.; Zeng, J.-J. Axial impact behavior of Large-Rupture-Strain (LRS) fiber reinforced polymer (FRP)-confined concrete cylinders. *Compos. Struct.* **2021**, *276*, 114563. [CrossRef]
19. Godat, A.; Aldaweela, S.; Aljaberi, H.; Al Tamimi, N.; Alghafri, E. Bond strength of FRP bars in recycled-aggregate concrete. *Constr. Build. Mater.* **2021**, *267*, 120919. [CrossRef]
20. Liu, S.; Bai, C.; Zhang, J.; Zhao, J.; Hu, Q. Experimental and theoretical study on bonding performance of FRP bars-Recycled aggregate concrete. *Constr. Build. Mater.* **2022**, *361*, 129614. [CrossRef]
21. Zhou, W.; Feng, P.; Lin, H.; Zhou, P. Bond behavior between GFRP bars and coral aggregate concrete. *Compos. Struct.* **2023**, *306*, 116567. [CrossRef]
22. Mai, G.; Li, L.; Lin, J.; Wei, W.; He, S.; Zhong, R.; Xiong, Z. Bond durability between BFRP bars and recycled aggregate seawater sea-sand concrete in freezing-thawing environment. *J. Build. Eng.* **2023**, *70*, 106422. [CrossRef]
23. Solyom, S.; Balázs, G.L. Bond of FRP bars with different surface characteristics. *Constr. Build. Mater.* **2020**, *264*, 119839. [CrossRef]
24. Fahmy, M.F.; Ahmed, S.A.; Wu, Z. Bar surface treatment effect on the bond-slip behavior and mechanism of basalt FRP bars embedded in concrete. *Constr. Build. Mater.* **2021**, *289*, 122844. [CrossRef]
25. Basaran, B.; Donmez, E.T. Effects of fibre wrapping degree and ratio on the tensile properties of carbon FRP-steel hybrid reinforcements. *J. Build. Eng.* **2023**, *76*, 107189. [CrossRef]
26. Chen, J.; Fang, Z.; Chen, X.; Jiang, R. Experimental study on lap behavior of CFRP indented bars in UHPC. *Constr. Build. Mater.* **2022**, *344*, 127959. [CrossRef]
27. Majain, N.; Rahman, A.B.A.; Adnan, A.; Mohamed, R.N. Pullout behaviour of ribbed bars in self-compacting concrete with steel fibers. *Mater. Today Proc.* **2021**, *39*, 1034–1040. [CrossRef]
28. Hao, Q.; Wang, Y.; He, Z.; Ou, J. Bond strength of glass fiber reinforced polymer ribbed rebars in normal strength concrete. *Constr. Build. Mater.* **2009**, *23*, 865–871. [CrossRef]
29. Wei, W.; Liu, F.; Xiong, Z.; Lu, Z.; Li, L. Bond performance between fibre-reinforced polymer bars and concrete under pull-out tests. *Constr. Build. Mater.* **2019**, *227*, 116803. [CrossRef]
30. Sasmal, S.; Khatri, C.P.; Ramanjaneyulu, K.; Srinivas, V. Numerical evaluation of bond–slip relations for near-surface mounted carbon fiber bars embedded in concrete. *Constr. Build. Mater.* **2013**, *40*, 1097–1109. [CrossRef]
31. Shan, Z.; Liang, K.; Chen, L. Bond behavior of helically wound FRP bars with different surface characteristics in fiber-reinforced concrete. *J. Build. Eng.* **2023**, *65*, 105504. [CrossRef]
32. El-Nemr, A.; Ahmed, E.A.; Barris, C.; Joyklad, P.; Hussain, Q.; Benmokrane, B. Bond performance of fiber reinforced polymer bars in normal- and high-strength concrete. *Constr. Build. Mater.* **2023**, *393*, 131957. [CrossRef]
33. Liang, K.; Chen, L.; Shan, Z.; Su, R. Experimental and theoretical study on bond behavior of helically wound FRP bars with different rib geometry embedded in ultra-high-performance concrete. *Eng. Struct.* **2023**, *281*, 115769. [CrossRef]
34. JSCE. *Recommendation Fordesign and Construction of Concrete Structures Using Continuous Fiber Reinforcing Materials*; Japan Society of Civil Engineers: Tokyo, Japan, 1997.
35. *CSA S806*; Design and Construction of Building Components with Fibre Reinforced Polymers. Canadian Standards Association: Rexdale, ON, USA, 2002.
36. *ACI 440*; 1R-Guide for the Design and Construction of Structural Concrete Reinforced with FRP Bars. American Concrete Institute: Farmington Hills, MI, USA, 2015.

37. Xiong, Z.; Wei, W.; He, S.; Liu, F.; Luo, H.; Li, L. Dynamic bond behaviour of fibre-wrapped basalt fibre-reinforced polymer bars embedded in sea sand and recycled aggregate concrete under high-strain rate pull-out tests. *Constr. Build. Mater.* **2021**, *276*, 122195. [CrossRef]
38. Lu, Z.; Su, L.; Lai, J.; Xie, J.; Yuan, B. Bond durability of BFRP bars embedded in concrete with fly ash in aggressive environments. *Compos. Struct.* **2021**, *271*, 114121. [CrossRef]
39. Yan, Z.-W.; Bai, Y.-L.; Ozbakkaloglu, T.; Gao, W.-Y.; Zeng, J.-J. Rate-dependent compressive behavior of concrete confined with Large-Rupture-Strain (LRS) FRP. *Compos. Struct.* **2021**, *272*, 114199. [CrossRef]
40. *JGJ 55-2011*; Specification for Mix Proportion Design of Ordinary Concrete. Ministry of Housing and Urban Rural Development of the People's Republic of China: Beijing, China, 2011.
41. *ASTM C39/C39M*; Standard Test Method for Compressive Strength of Cylinder Specimens. ASTM International: West Conshohocken, PA, USA, 2018.
42. *ASTM C469/C469M*; Standard Test Method for Static Modulus of Elasticity and Poisson's Ratio of Concrete in Compression. ASTM International: West Conshohocken, PA, USA, 2014.
43. *ACI 440.3R-12*; Guide Test Methods for Fiber-Reinforced Polymer (FRP) Composites for Reinforcing or Strengthening Concrete and Masonry Structures. American Concrete Institute: Farmington Hills, MI, USA, 2012.
44. Xiong, Z.; Zeng, Y.; Li, L.; Kwan, A.; He, S. Experimental study on the effects of glass fibres and expansive agent on the bond behaviour of glass/basalt FRP bars in seawater sea-sand concrete. *Constr. Build. Mater.* **2021**, *274*, 122100. [CrossRef]
45. Chen, L.; Liang, K.; Shan, Z. Experimental and theoretical studies on bond behavior between concrete and FRP bars with different surface conditions. *Compos. Struct.* **2023**, *309*, 116721. [CrossRef]
46. Otoom, O.F.; Lokuge, W.; Karunasena, W.; Manalo, A.C.; Ozbakkaloglu, T.; Ehsani, M.R. Flexural behaviour of circular reinforced concrete columns strengthened by glass fibre reinforced polymer wrapping system. *Structures* **2022**, *38*, 1326–1348. [CrossRef]
47. Al-Hamrani, A.; Alnahhal, W. Bond durability of sand coated and ribbed basalt FRP bars embedded in high-strength concrete. *Constr. Build. Mater.* **2023**, *406*, 133385. [CrossRef]
48. Ke, L.; Liang, L.; Feng, Z.; Li, C.; Zhou, J.; Li, Y. Bond performance of CFRP bars embedded in UHPFRC incorporating orientation and content of steel fibers. *J. Build. Eng.* **2023**, *73*, 106827. [CrossRef]